
Article:
Khan, RA orcid.org/0000-0002-2045-2237, Shepley, PM orcid.org/0000-0003-1240-593X, Hrabec, A et al. (4 more authors) (2016) Effect of annealing on the interfacial Dzyaloshinskii-Moriya interaction in Ta/CoFeB/MgO trilayers. Applied Physics Letters, 109 (13). 132404. ISSN 0003-6951

https://doi.org/10.1063/1.4963731

Effect of annealing on the interfacial Dzyaloshinskii-Moriya interaction in Ta/CoFeB/MgO trilayers

R. A. Khan,[1, a)] P. M. Shepley,[1] A. Hrabec,[1, b)] A. W. J. Wells,[1] B. Ocker,[2] C. H. Marrows,[1] and T. A. Moore[1]
[1)] *School of Physics and Astronomy, University of Leeds, Leeds LS2 9JT, United Kingdom*
[2)] *Singulus Technologies AG, 63796 Kahl am Main, Germany*

(Dated: 6 September 2016)

The interfacial Dzyaloshinskii-Moriya interaction (DMI) has been shown to stabilize homochiral Néel-type domain walls in thin films with perpendicular magnetic anisotropy and as a result permit them to be propagated by a spin Hall torque. In this study, we demonstrate that in Ta/$Co_{20}Fe_{60}B_{20}$/MgO the DMI may be influenced by annealing. We find that the DMI peaks at $D = 0.057 \pm 0.003$ mJ/m^2 at an annealing temperature of 230 °C. DMI fields were measured using a purely field-driven creep regime domain expansion technique. The DMI field and the anisotropy field follow a similar trend as a function of annealing temperature. We infer that the behavior of the DMI and the anisotropy are related to interfacial crystal ordering and B expulsion out of the CoFeB layer as the annealing temperature is increased.

In thin magnetic multilayers current-driven domain wall (DW) motion holds great potential for use in spintronic devices[1–3]. In multilayers with perpendicular magnetic anisotropy and structural inversion asymmetry DW motion is governed by various torques generated by spin-orbit effects, principally, the Rashba effect[4–6] and the spin Hall effect[7–9]. Furthermore, the presence of an antisymmetric exchange interaction, known as the Dzyaloshinskii-Moriya interaction (DMI)[10,11], is reported to influence the DW spin structure[12] and thus its current-driven dynamics[7,13–15]. Ta/CoFeB/MgO has been found to possess the DMI[16,17]. Current flowing in the Ta layer can generate spin-orbit torque via the spin Hall effect[18] that leads to magnetization switching of the CoFeB and DW motion[19].

Ta/CoFeB/MgO has a low density of DW pinning defects[20], and also forms part of a magnetic tunnel junction[21]. Thus, the prospect of efficient current-induced DW motion combined with readout via tunnel magnetoresistance makes it promising for low power memory or logic devices. Knowledge of the role of the DMI is essential for understanding current-induced DW dynamics in this material. The DMI originates at the heavy metal/ferromagnet interface where adjacent spins align through the exchange interaction mediated by a heavy atom with a large spin-orbit coupling. It manifests as an effective in-plane field, the DMI field, acting locally on a Bloch wall, which is magnetostatically favored, and converting it to a chiral Néel wall[22]. The chirality arises since the DMI field points in a specific direction as expressed by $-\mathbf{D} \cdot (\mathbf{S}_1 \times \mathbf{S}_2)$, where $\mathbf{S}_1$ and $\mathbf{S}_2$ are neighboring spins and $\mathbf{D}$ is the DM vector.

Here we report how the DMI is affected by thermal annealing in Ta/CoFeB/MgO thin films, since annealing is generally required to produce a strong perpendicular anisotropy in this system, and sample heating is often used in nanofabrication procedures. The DMI was measured using a field-driven DW creep method[14,23]. We report an optimum annealing temperature for a maximum DMI in this material system. We then discuss the possible underlying mechanisms with reference to the anisotropy field which was found to follow a similar behavior as a function of the annealing temperature.

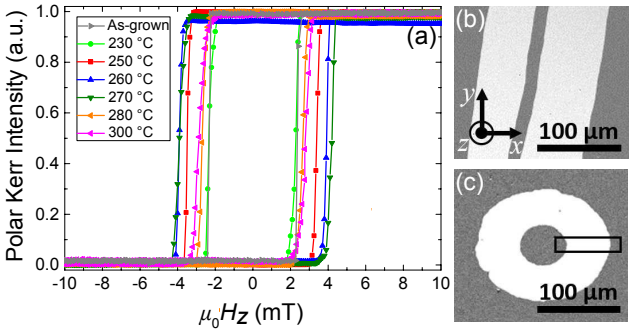

FIG. 1. (a) Polar MOKE hysteresis loops of Ta/CoFeB/MgO film for different annealing temperatures. Kerr microscope difference images showing the propagation of "line" domains (b) and "bubble" domains (c) after a field pulse. The bright regions represent the areas swept out by the DWs during the field pulse. The black rectangle in (c) marks an example of a section inside which DW velocities are measured in each pixel and averaged.

The material system consists of Ta(5 nm)/$Co_{20}Fe_{60}B_{20}$(0.8 nm)/MgO(2 nm) deposited on a thermally oxidized Si wafer. The multilayer was grown by sputtering using a Singulus TIMARIS/ROTARIS tool. A 5 nm capping layer of Ta was also deposited on top of the stack in order to prevent degradation of the MgO layer in ambient conditions and during annealing. The grown samples were then annealed at the desired temperature (ramp rate of 5 °C/min) for 2 hrs in vacuum at a pressure of approximately 10^{-5} mbar. The as-deposited and the annealed samples all exhibit a uniaxial magnetic anisotropy perpendicular to the plane of the sample. This is shown by the square

[a)] Correspondence: pyrak@leeds.ac.uk
[b)] Now at Laboratoire de Physique des Solides, CNRS, Orsay, France

magnetic hysteresis loops (FIG. 1(a)) measured by polar magneto-optic Kerr effect (MOKE) magnetometry. The as-deposited film shows "line" domains (FIG. 1(b)), whereas, the same film when annealed at 200 °C exhibits "bubble" domains (FIG. 1(c)). Line domains occur when an as-grown film is incompletely saturated, and reversal starts from two closely-spaced homochiral DWs[12]. In order to initialize a domain configuration, the film is first saturated in one direction. Then, a reverse field is applied to prepare a domain, either from one of the pre-reversed lines, or from a bubble at a defect. In the present study, we measure the DMI only from annealed films where bubble domains are nucleated. The domains were imaged using a wide field Kerr microscope equipped with two electromagnets to generate an in-plane (IP) and an out-of-plane (OOP) magnetic field simultaneously. Images captured before and after a field pulse were subtracted. DW displacement is measured from the difference image and the corresponding DW velocity is calculated by normalizing the displacement by the pulse time. To reduce uncertainties, velocities were calculated for each pixel of a section (black rectangle) and averaged. This procedure was then repeated at least three times with different pulse times and further averaged.

The DMI field is measured using a field-driven DW creep method[14,23]. Using field alone avoids the possibility of mixing with current-related effects. In the case of a reverse nucleated circular bubble domain, the DMI field H_{DMI} acts on the DW where it maintains radial symmetry with respect to the axis of expansion, which is parallel to the OOP field direction (z-axis in this case). Thus, the circular domain expands in an isotropic way when an OOP field H_z is applied, as demonstrated by FIG. 2(a). The symmetry is broken (FIG. 2(b)) when the OOP expansion is performed but in the presence of an applied IP field H_x. This is because the applied IP field either adds to the DMI field (right side in this case), or opposes it (left side). Thus, the effective IP field acting on the DW is enhanced ($H_x + H_{\mathrm{DMI}}$) on one side, causing an increase in the velocity, compared to the DW velocity on the other side where the effective field is diminished ($H_x - H_{\mathrm{DMI}}$).

The effect of the DMI field on the DW velocity can be readily observed by plotting the DW velocity as a function of IP field H_x, for a fixed OOP field which drives the DW. FIG. 2(c) shows the data for a sample which has been annealed at 280 °C. It can be seen that the two DW velocity plots (red and blue for DWs moving right and left, respectively) shift away from $H_x = 0$ in opposite directions. We take the offset of the minimum from $H_x = 0$ as a measure of H_{DMI} since at this point H_x exactly cancels out H_{DMI} resulting in the lowest DW velocity. This velocity is non-zero since the OOP field is still driving the DW. The minimum velocity, and therefore H_{DMI} can be easily identified from the plot without the need of any further analysis. However, in order to identify H_{DMI} to a high degree of precision, the data points are fitted with the creep law of DW dynamics, which

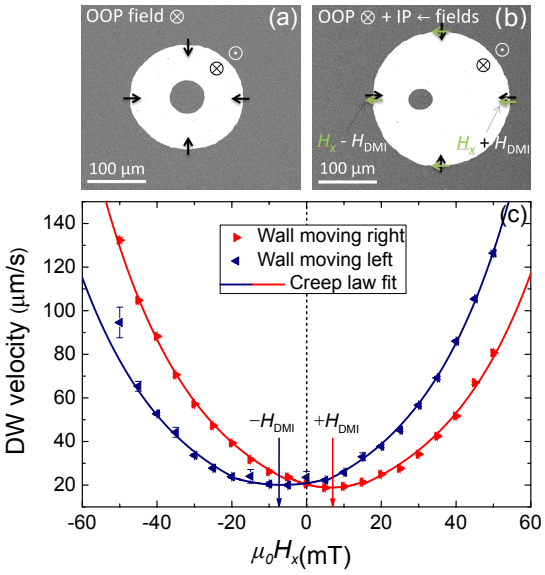

FIG. 2. Kerr microscope difference images showing: (a) isotropic expansion of a nucleated bubble domain by an OOP field pulse H_z. The bright region represents the area swept out by an up-down DW during the field pulse. The black arrows represent the orientation of spins in the center of an ideal Néel type DW due to the intrinsic DMI field H_{DMI}; (b) asymmetric expansion when the same method is performed but in presence of a static IP field H_x. The green arrows represent the action of the IP field on the DW spins. (c) DW velocity as a function of IP field H_x where the DW was driven with an OOP field pulse H_z of 1.4 mT. The error bars are from standard deviations of the average values. The solid lines are fits of the creep scaling law, Equation (1). The minimum points of the plots mark the DMI fields H_{DMI} indicated by the arrows.

assumes that the DW is a 1D elastic interface moving in a 2D weakly disordered medium and that its velocity increases exponentially as a function of the driving force[24,25]. The creep law is expressed as:

$$v = v_0 \exp[-\zeta(\mu_0 H_z)^{-\mu}], \tag{1}$$

where μ is the creep exponent which takes the value of 1/4 for field-driven DW motion[24,26,27], the prefactor v_0 is the characteristic speed, and ζ is a scaling factor and is expressed as:

$$\zeta = \zeta_0[\sigma(H_x)/\sigma(0)]^{1/4}, \tag{2}$$

where ζ_0 is a scaling constant and σ is the DW energy density. The constants v_0 and ζ_0 were extracted from the intercept and gradient of a linear fit of the plot of $\ln v$ vs $(H_z)^{-1/4}$ at $H_x = 0$.

The DW energy density σ is a function of the applied IP field H_x[23], and takes the form of

$$\sigma(H_x) = \sigma_0 - \frac{\pi^2 \Delta \mu_0^2 M_{\mathrm{s}}^2}{8K_{\mathrm{D}}}(H_x + H_{\mathrm{DMI}})^2 \tag{3}$$

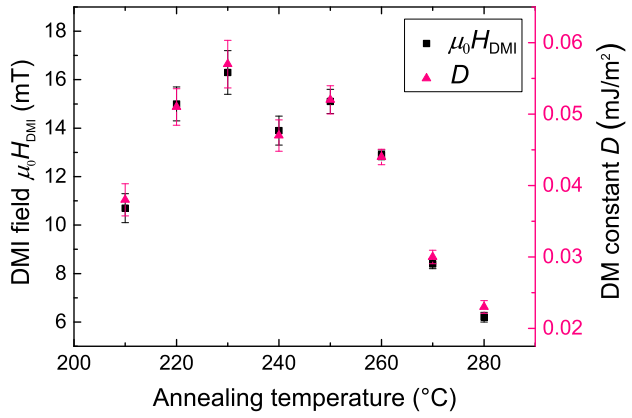

FIG. 3. Plot of the DMI field $\mu_0 H_{\rm DMI}$ (black squares) and the DM constant D (pink triangles) as a function of annealing temperature. The uncertainties in the DMI fields are from standard deviations of the averages.

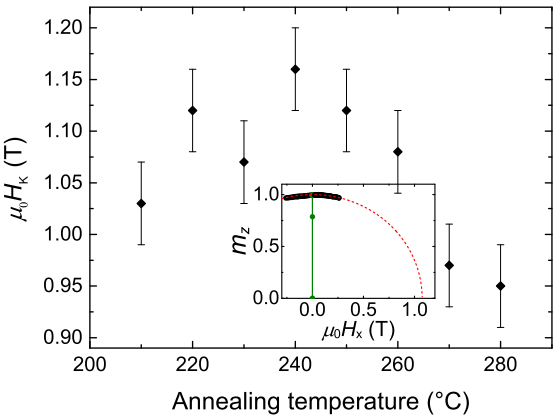

FIG. 4. Effective anisotropy field $\mu_0 H_{\rm K}$ vs annealing temperature. Inset: Plot of (normalized) OOP magnetization m_z vs IP field $\mu_0 H_x$. The OOP magnetization was probed using a Kerr microscope in the polar settings. Before applying the IP field, the magnetization was saturated along the easy z-axis using an OOP field $\mu_0 H_z$ (green data points). This ensured a maximum value of m_z, while $m_x = 0$. The red dashed line is the extrapolation of the plot assuming that the magnetization rotates coherently as the IP field is increased. Hence, the x-intercept represents the anisotropy field.

for the condition $|H_x + H_{\rm DMI}| < 4K_{\rm D}/\pi\mu_0 M_{\rm s}$. This is when the effective IP field acting on the DW ($H_x + H_{\rm DMI}$) is not sufficient to completely transform a Bloch wall into a Néel wall, i.e. at relatively low applied IP fields. In this scenario the spin structure of the DW is in a Bloch-Néel mixed state. Otherwise, when a DW is fully transformed into a Néel wall, the DW energy density is expressed as:

$$\sigma(H_x) = \sigma_0 + 2K_{\rm D}\Delta - \pi\Delta\mu_0 M_{\rm s}|H_x + H_{\rm DMI}|. \qquad (4)$$

In these expressions, σ_0 is the Bloch wall energy density and is expressed as $\sigma_0 = 4\sqrt{AK_0}$, where A is the exchange stiffness, taken to be 10 pJ/m, and $K_0 = \mu_0 H_{\rm K} M_{\rm s}/2$ is the effective anisotropy, where $\mu_0 H_{\rm K}$ is the measured effective anisotropy field (discussed later); $\Delta = \sqrt{A/K_0}$ is the DW width; $M_{\rm s} = (6.50 \pm 0.04) \times 10^5$ A/m is the saturation magnetization and is measured by a Quantum Design SQUID-VSM; $K_{\rm D} = N_x \mu_0 M_{\rm s}^2/2$ is the magnetostatic shape anisotropy of the wall with N_x as the demagnetization prefactor[28]. FIG. 2(c) shows that the experimental data fits well with the DW creep model (solid lines). This model was fitted to the data for all the samples annealed at different temperatures. The DMI fields were consequently extracted from the fits. We then calculated the effective DM constant D by using the expression[13] $D = \mu_0 H_{\rm DMI} M_{\rm s} \Delta$.

FIG. 3 shows how the magnitude of the DMI field $H_{\rm DMI}$ (black) and subsequently the DM constant D (pink) varies as a function of annealing temperature. We find that the DMI gradually rises from $D = 0.038 \pm 0.002$ mJ/m^2 at a temperature of 210 °C, reaches a peak value of $D = 0.057 \pm 0.003$ mJ/m^2 at 230 °C, and then decreases as the temperature is increased further.

The anisotropy field $\mu_0 H_{\rm K}$ is measured magneto-optically for a low field range over which the magnetization rotates coherently. In this method, as illustrated in FIG. 4 (inset), the Kerr microscope is set up in the polar configuration so that the OOP component of the magnetization m_z is probed. In this configuration, m_z is measured continuously while an IP field H_x is applied to rotate the magnetization from the easy (OOP) to the hard axis (IP)[29]. At $H_x = 0$, the magnetization is saturated in the z-direction (easy axis) using an OOP field H_z (green points) resulting in the maximum value of m_z (while $m_x = 0$). Now as H_x is increased, the magnetization starts to rotate towards the x-direction (hard axis) and thus m_z gets smaller in magnitude until nucleation of domains starts to occur causing a sharp drop in m_z (not shown). Thus, the low field data is extrapolated to obtain the anisotropy field from the x-intercept assuming that the magnetization rotates coherently, i.e. $\mathbf{m} = m_z^2 + m_x^2 = 1$, within this low field regime. The uncertainty is obtained from the quality of the fit and by performing repeated measurements.

We find that the anisotropy field follows a similar trend (FIG. 4) as the DMI, with regard to the annealing temperature, peaking in magnitude at about the same temperature as the DMI peak. Such a behavior of the anisotropy field was also reported by Avci *et al.*[30], although for a smaller temperature range. The initial rise in the anisotropy field is due to an increase in the crystal ordering of the CoFeB and MgO layers due to annealing[31,32]. Crystallization of the CoFeB layer is also brought about by the diffusion of B, due to annealing, out of the CoFeB and into the adjacent layers. This was reported by Lo Conte *et al.* through chemical depth profiling[16]. An increased ordering of these two layers

leads to a rise in the anisotropies at the MgO/CoFeB and CoFeB/Ta interfaces, both of which contribute to the PMA of the stack. However, further increasing the annealing temperature causes a decrease in the magnetic anisotropy. We attribute this to a combined effect of B deposition[16], and intermixing[32] at both the MgO/CoFeB and CoFeB/Ta interfaces due to annealing at relatively high temperatures.

Since the DMI and the anisotropy field follow a similar trend with respect to the annealing temperature, we infer that similar mechanisms underpin both these phenomena. Since the DMI is sensitive to the atomic arrangements at the interface[14,33], an improved ordering of the atoms at the Ta/CoFeB interface brought about by annealing is the reason for the initial enhancement of the DMI. At higher annealing temperatures the accumulation of B at the Ta/CoFeB interface becomes significant and essentially weakens the interaction between the atoms of the Ta and the CoFeB layers. Furthermore, annealing at higher temperatures also leads to intermixing at the interface which has been reported[34] to be detrimental for the DMI. Thus, these two factors together contribute to the lowering of the strength of the DMI at relatively high annealing temperatures.

The obtained magnitude and sign of D agrees well with previous reports[16,17] on Ta/CoFeB/MgO stacks. The chirality of the DW can be deduced from the directions of the OOP and IP fields. The DWs in this system are determined to have a right-handed chirality and thus the sign of D is positive.

In conclusion, we have demonstrated how the interfacial DMI in Ta(5 nm)/$Co_{20}Fe_{60}B_{20}$(0.8 nm)/MgO(2 nm) multilayer is affected by annealing temperature. We measured DMI fields via the field-driven expansion of magnetic domains and found that the DMI peaks at $D = 0.057 \pm 0.003$ mJ/m^2 at a temperature of 230 °C. This behavior is related to interfacial crystal ordering and segregation of B out of the CoFeB layer and consequent accumulation at the Ta/CoFeB interface, as the anisotropy field is found to follow a similar trend and peaks in magnitude at around the same temperature as the DMI field.

This work has been funded by the European Community under the Marie-Curie Seventh Framework program - ITN "WALL"(Grant no. 608031). Equipment funding has been provided by U.K. EPSRC; Grant no. EP/K003127/1 for the Kerr Microscope, and Grant no. EP/K00512X/1 for the SQUID-VSM. The authors would like to thank O. Cespedes and G. Burnell for helpful discussions.

[1]S. S. P. Parkin, M. Hayashi, and L. Thomas, Science **320**, 190–194 (2008).
[2]D. A. Allwood, G. Xiong, C. C. Faulkner, D. Atkinson, D. Petit, and R. P. Cowburn, Science **309**, 1688–1692 (2005).
[3]S. Fukami, T. Suzuki, K. Nagahara, N. Ohshima, Y. Ozaki, S. Saito, R. Nebashi, N. Sakimura, H. Honjo, K. Mori, *et al.*, in *2009 Symposium on VLSI Technology* (2009).
[4]I. M. Miron, G. Gaudin, S. Auffret, B. Rodmacq, A. Schuhl, S. Pizzini, J. Vogel, and P. Gambardella, Nature Materials **9**, 230–234 (2010).
[5]Y. A. Bychkov and E. I. Rashba, Journal of Physics C: Solid State Physics **17**, 6039 (1984).
[6]I. M. Miron, T. A. Moore, H. Szambolics, L. D. Buda-Prejbeanu, S. Auffret, B. Rodmacq, S. Pizzini, J. Vogel, M. Bonfim, A. Schuhl, *et al.*, Nature Materials **10**, 419–423 (2011).
[7]S. Emori, U. Bauer, S.-M. Ahn, E. Martinez, and G. S. D. Beach, Nature Materials **12**, 611–616 (2013).
[8]L. Liu, O. J. Lee, T. J. Gudmundsen, D. C. Ralph, and R. A. Buhrman, Physical Review Letters **109**, 096602 (2012).
[9]M. I. Dyakonov and V. I. Perel, Physics Letters A **35**, 459–460 (1971).
[10]I. Dzyaloshinsky, Journal of Physics and Chemistry of Solids **4**, 241–255 (1958).
[11]T. Moriya, Physical Review **120**, 91 (1960).
[12]M. J. Benitez, A. Hrabec, A. P. Mihai, T. A. Moore, G. Burnell, D. McGrouther, C. H. Marrows, and S. McVitie, Nature Communications **6**, 8957 (2015).
[13]A. Thiaville, S. Rohart, É. Jué, V. Cros, and A. Fert, EPL (Europhysics Letters) **100**, 57002 (2012).
[14]A. Hrabec, N. A. Porter, A. Wells, M. J. Benitez, G. Burnell, S. McVitie, D. McGrouther, T. A. Moore, and C. H. Marrows, Physical Review B **90**, 020402 (2014).
[15]K.-S. Ryu, L. Thomas, S.-H. Yang, and S. Parkin, Nature Nanotechnology **8**, 527–533 (2013).
[16]R. Lo Conte, E. Martinez, A. Hrabec, A. Lamperti, T. Schulz, L. Nasi, L. Lazzarini, R. Mantovan, F. Maccherozzi, S. S. Dhesi, *et al.*, Physical Review B **91**, 014433 (2015).
[17]J. Torrejon, J. Kim, J. Sinha, S. Mitani, M. Hayashi, M. Yamanouchi, and H. Ohno, Nature communications **5**, 4655 (2014).
[18]L. Liu, C.-F. Pai, Y. Li, H. W. Tseng, D. C. Ralph, and R. A. Buhrman, Science **336**, 555–558 (2012).
[19]R. Lo Conte, A. Hrabec, A. P. Mihai, T. Schulz, S.-J. Noh, C. H. Marrows, T. A. Moore, and M. Kläui, Applied Physics Letters **105**, 122404 (2014).
[20]C. Burrowes, N. Vernier, J.-P. Adam, L. H. Diez, K. Garcia, I. Barisic, G. Agnus, S. Eimer, J.-V. Kim, T. Devolder, *et al.*, Applied Physics Letters **103**, 182401 (2013).
[21]S. Ikeda, K. Miura, H. Yamamoto, K. Mizunuma, H. Gan, M. Endo, S. Kanai, J. Hayakawa, F. Matsukura, and H. Ohno, Nature materials **9**, 721–724 (2010).
[22]G. Chen, J. Zhu, A. Quesada, J. Li, A. T. NDiaye, Y. Huo, T. P. Ma, Y. Chen, H. Y. Kwon, C. Won, *et al.*, Physical Review Letters **110**, 177204 (2013).
[23]S.-G. Je, D.-H. Kim, S.-C. Yoo, B.-C. Min, K.-J. Lee, and S.-B. Choe, Physical Review B **88**, 214401 (2013).
[24]S. Lemerle, J. Ferré, C. Chappert, V. Mathet, T. Giamarchi, and P. Le Doussal, Physical Review Letters **80**, 849 (1998).
[25]P. Chauve, T. Giamarchi, and P. Le Doussal, Physical Review B **62**, 6241 (2000).
[26]K.-J. Kim, J.-C. Lee, S.-M. Ahn, K.-S. Lee, C.-W. Lee, Y. J. Cho, S. Seo, K.-H. Shin, S.-B. Choe, and H.-W. Lee, Nature **458**, 740–742 (2009).
[27]P. J. Metaxas, J. P. Jamet, A. Mougin, M. Cormier, J. Ferré, V. Baltz, B. Rodmacq, B. Dieny, and R. L. Stamps, Physical Review Letters **99**, 217208 (2007).
[28]S. V. Tarasenko, A. Stankiewicz, V. V. Tarasenko, and J. Ferré, Journal of magnetism and magnetic materials **189**, 19–24 (1998).
[29]P. M. Shepley, A. W. Rushforth, M. Wang, G. Burnell, and T. A. Moore, Scientific Reports **5**, 7921 (2015).
[30]C. O. Avci, K. Garello, C. Nistor, S. Godey, B. Ballesteros, A. Mugarza, A. Barla, M. Valvidares, E. Pellegrin, A. Ghosh, *et al.*, Physical Review B **89**, 214419 (2014).
[31]S. Cardoso, C. Cavaco, R. Ferreira, L. Pereira, M. Rickart, P. P. Freitas, N. Franco, J. Gouveia, and N. P. Barradas, Journal of Applied Physics **97**, 10C916–10C916 (2005).
[32]B. Cui, C. Song, G. Y. Wang, Y. Y. Wang, F. Zeng, and F. Pan, Journal of Alloys and Compounds **559**, 112–115 (2013).
[33]R. Lavrijsen, D. M. F. Hartmann, A. van den Brink, Y. Yin,

B. Barcones, R. A. Duine, M. A. Verheijen, H. J. M. Swagten, and B. Koopmans, Physical Review B **91**, 104414 (2015).

[34]H. Yang, A. Thiaville, S. Rohart, A. Fert, and M. Chshiev, Physical Review Letters **115**, 267210 (2015).